Regolith mixing by impacts: Lateral diffusion of basin melt

Tiantian Liu[1,2], Greg Michael[2], Juliane Engelmann[2,3], Kai Wünneman[2,3], Jürgen Oberst[1,4]

1 Institute of Geodesy and Geoinformation Science, Technische Universität Berlin, 10623 Berlin, Germany (tiantian.liu@tu-berlin.de)

2 Freie Universität Berlin, Malteserstr., 74-100, Haus D, 12249 Berlin, Germany

3 Museum für Naturkunde, Leibniz Institute for Evolution and Biodiversity Science, 10115 Berlin, Germany

4 Institute of Planetary Research, German Aerospace Center (DLR), 12489 Berlin, Germany

Key Words

Moon, surface; regoliths; impact processes; cratering

Abstract

Impact cratering has been the primary process to alter the distribution of lunar highland material since the formation of a crust. This impact history is recorded in the radiogenic clocks of impact melts which are accessible for study on lunar samples and meteorites. However, primary impact melt is exposed to a long-time gardening process (i.e. re-melting, excavation, burial, and re-excavation) by subsequent impacts resulting in a complex spatial distribution of materials representing specific impact events. To investigate the diffusion behavior of impact melt, a model tracing the evolving distribution of melt laterally and with depth was built using a Monte Carlo approach. Given scaling laws concerning melt production and ejecta distribution, the size-frequency distribution of impact craters, and the rate function for crater formation, we examine the evolution of melt component occurrence of different ages. Three mid- to late-forming basins (Serenitatis, Crisium, and Imbrium) are chosen as a case study for the diffusion of melt from major basin-forming events. The survival probability of basin

melt occurrence at the Apollo and Luna sampling spots is derived. It is expected to find abundant Imbrium and Crisium melt at the Apollo and Luna sampling sites, consistent with the K-Ar radiometric dates of highland samples; whereas the older Serenitatis melt was subjected to the later long-term gardening, strongly influenced by later local impacts, and thus is less abundant. Understanding the diffusion of impact melt is helpful for interpretation of radiometric ages of lunar samples and can be used to predict the distribution of differently-aged melts at future landing/sampling sites such as the Chinese Chang'E-4 (CE-4).

1 Introduction

Impact cratering has been the primary process modifying the lunar surface since the formation of the lunar crust (Hörz et al. 1991). Shock compression generated by impact deposits part of the energy budget as heat in the target rocks during unloading. If the temperature excursion exceeds the normal melting points of the target rocks, the material becomes molten (French 1998; Melosh 1989; Stöffler et al. 2017). The subsequent dynamic processes of impact excavation leave the majority of the impact melt distributed along the crater wall, with the remainder being ejected outside the crater in the form of a mixed layer of melted and unheated materials (Melosh 1989; Osinski & Pierazzo 2012). The radiometric clocks, e.g. K-Ar, of melted materials are reset leaving a record in the affected rocks (e.g., suevitic impact breccia and melt lens), which can be deciphered by means of isotopic dating techniques from collected lunar samples or meteorites (Flude et al. 2014; McDougall & Harrison 1999; Wilhelms 1987). The radiometric dating of impact melt and its association to particular impact events on the Moon is key to our understanding of lunar chronology.

The impact melt emplaced by one event is gardened (i.e. re-melted, excavated, buried, and re-excavated) by later events which alter the original melt distribution both laterally and with depth, as well as diminishing its total presence by reheating. Previous studies, both by analytical and numerical methods, provide various scaling laws to determine the melt production during a single event (e.g., Ahrens & O'Keefe 1977; Cintala & Grieve 1998; Maher 1988; O'Keefe & Ahrens 1977; Pierazzo et al. 1997; Tonks & Melosh 1993; Wünnemann et al. 2008). However, the cumulative effect of a long sequence of impacts that produces a megaregolith is complex and not well-studied.

Recently, Michael et al. (2018) built a model to investigate such a long sequence of impact gardening using a Monte Carlo approach. The model considered melt abundances in an average sense over the lunar surface, attempting to illustrate the variation in abundance of differently aged melt components with depth. The obtained melt age histogram with several peaks resulting from basin events shows that a cataclysm is not required to reproduce the observations. However, that model was unable to address the variation of abundances with respect to a specific location on the lunar surface, which is the aim of this current work.

Lunar sample radiometric ages combined with their inferred origins tell us the ages of certain lunar terrains. These are essential constraints for diverse models regarding lunar bombardment history - a subject of enduring debate. The classic tail-end crater chronology models, where the impact flux declines exponentially over the first billion years of lunar history, was postulated by comparing the crater density over these terrains (Hartmann 1970; Neukum 1983; Neukum & Ivanov 1994; Neukum et al. 2001). Based on the hypothesized dynamic evolution of the Solar System or geochemical constrains from lunar samples, various models were proposed, such as cataclysm (Cohen 2000; Tera et al. 1974; Ryder 2001), saw-tooth (Morbidelli et al. 2012; Morbidelli et al. 2018), and the smashing asteroids model (Turner et al. 1973). No matter what method they used, all the model results had to explain the sample ages. Major peaks in the radiometric ages obtained from the lunar samples are believed to be related to the adjacent giant basin-forming events (Haskin et al. 1998; Michael et al. 2018; Ryder et al. 1989), although many have argued that the 3.9 Ga peak is an indicator of a period of late heavy bombardment. The quantitative estimation of the abundance of basin melt and understanding of its gardening processes may be used to invert the observed melt components to gain new constraints on the impact rate function.

In addition, an understanding of the melt gardening process can be applied to estimate the expected abundances of basin melt components at potential sampling/landing sites for future missions. This year's Chinese Chang'E-4 (CE-4) mission will explore the farside of the Moon where no previous missions have landed (J. Huang et al. 2018; Wu et al. 2017). In particular, the South Pole-Aitken (SPA) basin was chosen as the potential landing region. SPA basin is one of the largest impact features in the Solar System and is the oldest observable feature. The probability of finding SPA melt at the potential sampling site can be calculated with an understanding of gardening process.

In section 2, we describe how we developed the model to simulate gardening process. We simplified the model to two dimensions (2D) due to the complexity of melt component during the cumulative gardening process. In section 3, the migration of impact melt and the influence of the crater size-frequency distribution (SFD) on melt distribution are presented. Three mid- to late-forming giant basin events (Serenitatis, Crisium and Imbrium) were chosen for the modelling to study the diffusion of these basins' melt. In section 4, the characteristics of basin melt diffusion are first presented (section 4.1). The abundance of basin melt at Apollo and Luna sampling sites is then estimated and compared with the K-Ar radiometric ages from highland samples in section 4.2. Combining the results from both sections 4.1 and 4.2, the abundance of basin melt components at the potential landing site of the future CE-4 lunar mission is estimated. Some feasible suggestions are provided for sampling the potentially present melt material (section 4.3). In section 4.4, other factors influencing the distribution of melt are discussed, which should be considered for future models.

2 Model

The high temperatures and pressures caused by hypervelocity impact events on the Moon result in the melting of a fraction of the target materials. Such thermal events reset the radiometric clocks of the melted materials. The potassium-argon (K-Ar) clock is widely used in dating impact melt since it is easily reset by thermal events (McDougall & Harrison 1999; Flude et al. 2014; Jourdan et al. 2014; Wartho et al. 2014). High temperatures allow the decay product, Ar, to escape from the mother rocks as gas, which resets the system. Resetting ages can then be calculated by measuring the ratio of Ar to K concentrations. It should be noted that, in this study, when we use the term 'melt', it should be understood here to include material which has been heated above the K-Ar reset threshold, but has not reached the melting point. The K-Ar clock reset is the measurable property that we aim to trace with the model.

Once impact melt has been generated, it is gardened by subsequent impact events diminishing its abundance and spreading it more widely. A schematic of the gardening process is shown in Figure 1 where the target is shown to experience two impact events. During the first impact, when time is t_1, a fraction of the old unheated materials of the target (white color in Figure 1) is excavated and melted. The radiometric clock of the melted material, that is the melt age, is reset to t_1 shown as a red color in Figure 1a. Part of the generated melt stays within the crater, and the remainder is ejected in the form of a mixed layer consisting of the newly melted material and the old unheated material, that becomes the ejecta blanket shown in Figure 1b (Melosh 1989). The thickness of the ejecta blanket decreases with distance from the crater center whereas the fraction of melt in the ejecta increases (Figure 1b, Melosh 1989). At time t_2, a subsequent impact event occurs. It penetrates the previous ejecta blanket and excavates material from both the previous layer and beneath, melting a fraction of both (blue color in Figure 1c). Partial ejecta materials overlay the previous deposits (arrow in Figure 1d) leading to a locally more complex melt component structure. As more impact events occur on the lunar surface, a complex spatial distribution of differently aged melt components develops.

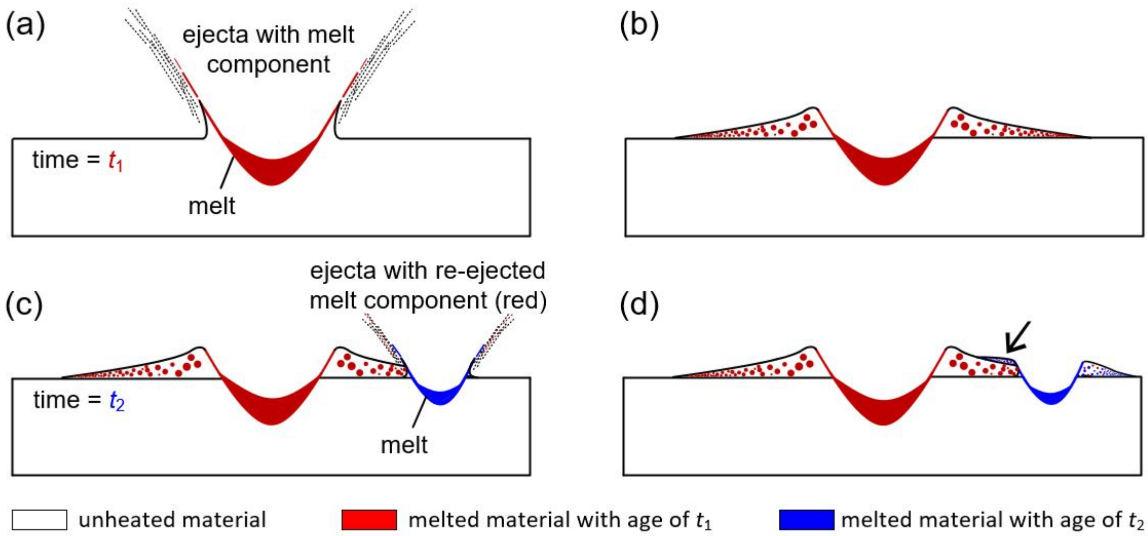

Figure 1. Schematic of the model where the white represents unheated material, red is the impact melt generated from the first impact event when time is t_1, and blue is melt from the second impact at time t_2. The arrow in Figure 1d points at the region of superposing ejecta.

2.1 Model steps

As seen from Figure 1, there are three key aspects which we considered when modelling the gardening process: the *distribution of impact events*, the *excavation processes*, and the *distribution of melted materials*.

Distribution of impact events: Due to the computational expense of the exponentially increasing number of simulated events as smaller impacts are included, a minimum crater diameter, D_{min}, is chosen. The maximum simulated diameter, D_{max}, is taken as 300 km, because this is the upper limit of the defined production function (PF) (Neukum 1983). Unless noted otherwise, diameters here refer to the rim-to-rim distance of observed craters. By using the Monte Carlo method, the diameter of craters, D, is generated, in such a way that the SFD of the generated impact craters statistically conforms to the PF larger than D_{min} (Michael et al. 2016). The corresponding center of each impact crater is randomly distributed along a line. The average time to the next impact event larger than D_{min} in diameter, or impact rate, is calculated from the chronology function (CF) (Neukum, 1983), PF, and t (see Michael et al. 2018 for the detail).

Excavating processes: The excavation depth for each simulated crater, d_{exc}, is $D_t/10$ where D_t is the diameter of transient crater (Melosh 1989). There are many scaling laws for D and D_t (Croft 1985; Holsapple 1993; Krüger et al. 2017; Melosh 1989; McKinnon et al. 1997). We choose the standard ones in this study: for simple craters, $D_t = 0.8D$ (Melosh 1989); and for complex craters, $D_t = (DD_Q^{0.13}/1.17)^{1/1.13}$ (McKinnon et al. 1997), where D_Q is the simple-complex transition diameter, and taken as 21 km (Pike 1977). The corresponding volume of the excavated materials having a torus-like shape (grey zone in Figure 2) is estimated to be 1/3 of a disc with d_{exc} in thickness and D_t in diameter (zone filled with black slash in Figure 2): $V_{exc} = \pi R_t^3/15$, where R_t is the radius of impact craters and equal to half of D_t. The excavation unit is assumed to be a cuboid with 1/3 D_t in length and d_{exc} in thickness located at the crater center. For the conservation of mass, the volume of each penetrated layer is diminished.

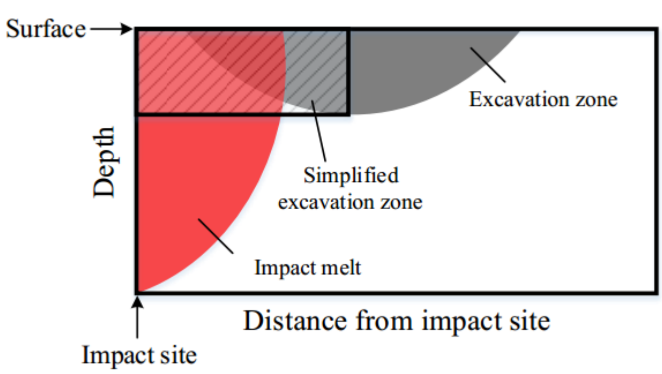

Figure 2 Schematic showing typical geometry of melting zone in iSALE modeling, with the impact-induced melt zone (red) and excavation zone in half space (grey, after Zhu et al. 2015). The calculation

of V_{exc} in this study is on the basis of the simplified excavation zone shown as an area that filled with black slash.

Distribution of melt materials: The thickness of the ejecta layer decreases with distance from crater center, r: δ (r) = Ar^{-3} (Hörz et al. 1983; Stöffler et al. 1975; Shuvalov & Dypvik 2013; Zhu et al. 2015), where A varies for craters with different D. To ensure conservation of mass, the integrated volume within five radii is taken to be exactly V_{exc}, based on which the variable A can be easily obtained for each differently-sized impact. The total volume of the generated impact melt with a reset age of the current model time is: $V_{melt} = cD_t^d$, where c and d are taken as 1.4×10^{-4} and 3.85, respectively (after Cintala & Grieve, 1998). The impact-induced melt zone during a single impact event is shown in Figure 2.

The distribution of material that experienced different degrees of shock pressure (including melt) is not well quantified and no scaling laws exist (Stöffler et al. 1975; Wünnemann et al. 2016). Recently, the linear relationship between the melt fraction in the proximal ejecta and the distance from crater center was found by means of numerical modelling using the iSALE shock-physics code (Wünnemann et al. 2006). In their model, basalt projectiles with diameters from 2.5 km to 10 km vertically impact a homogeneous target (same material as projectiles) at various impact velocities from 15 to 18 km/s, typical for the Moon. The transient crater radius of the generated impact crater ranges from 33 km to 107 km. By assuming a continual distribution of melt in the proximal ejecta, the thickness of the impact melt, δ_m, was obtained by multiplying the ejecta thickness with the melt proportion. It showed that the melt thickness decreases as a power law with increasing distance from the crater center. The exponent is approximately equal to -2: $\delta_m(r) = A_m r^{-2}$. A_m is recalculated for craters with different sizes to conserve V_{melt}, similarly to A described above, by taking the integrated melt volume within five radii to be exactly V_{melt}. The melt ratio, f_{melt}, at r is therefore equal to $\delta_m(r)\,/\delta\,(r)$. The amount of impact melt that is ejected from the crater depends on the transient crater size. According to Cintala & Grieve (1998), who combined different scaling relationships to estimate the ejected melt fraction, the amount of melt that remains inside the crater varies between 30% and 70% (assuming different scaling parameters, and crater sizes up to 400 km). In iSALE models for a projectile size range of 20 – 1000 m and an impact velocity of 20 km/s, only 80 – 90% of melt remain inside the crater. Therefore, we decided to use an intermediate value of 75%. Despite being a significant approximation, we believe this should be close enough to allow us to build up a qualitatively accurate view of the melt redistribution through multiple impacts. In addition, we treat the melt that is deposited inside the craters as a simple lens, although the exact distribution is likely more complex. About 85% of the ejected material is deposited within five radii from the crater center, the region that consists of a proximal ejecta blanket and a transition to a patchy discontinuous ejecta zone. We assume that the ejecta material in patchy transition zones is also continually distributed in a thin layer, and trace the melt only out to five radii from the crater center.

Figure 3 shows the ejecta and melt distribution of craters with diameters of 300, 100, and 5 km (dashed lines). It shows that the equivalent thicknesses – the components are mixed – of both the ejecta and melt decreases dramatically with distance from the crater center, and that larger craters produce a thicker layer within the five radii range (Figure 3a and b). The melt fraction of the largest crater (black dashed line in Figure 3c) is obviously greater than that of the smaller ones, and the farther from the crater rims, the greater the difference in the fraction of melt. When near the crater rim, the percentage of melt for 300-km, 100-km, and 5-km craters is 6.1%, 2.7%, and 0.2%, respectively; at five radii away from the crater center, the percentage of melt for 300-km, 100-km, and 5-km craters is 28.7%, 12.6%, and 1.1%, respectively.

Iteration: If t is less than zero – the present day – another impact is generated, repeating the above steps.

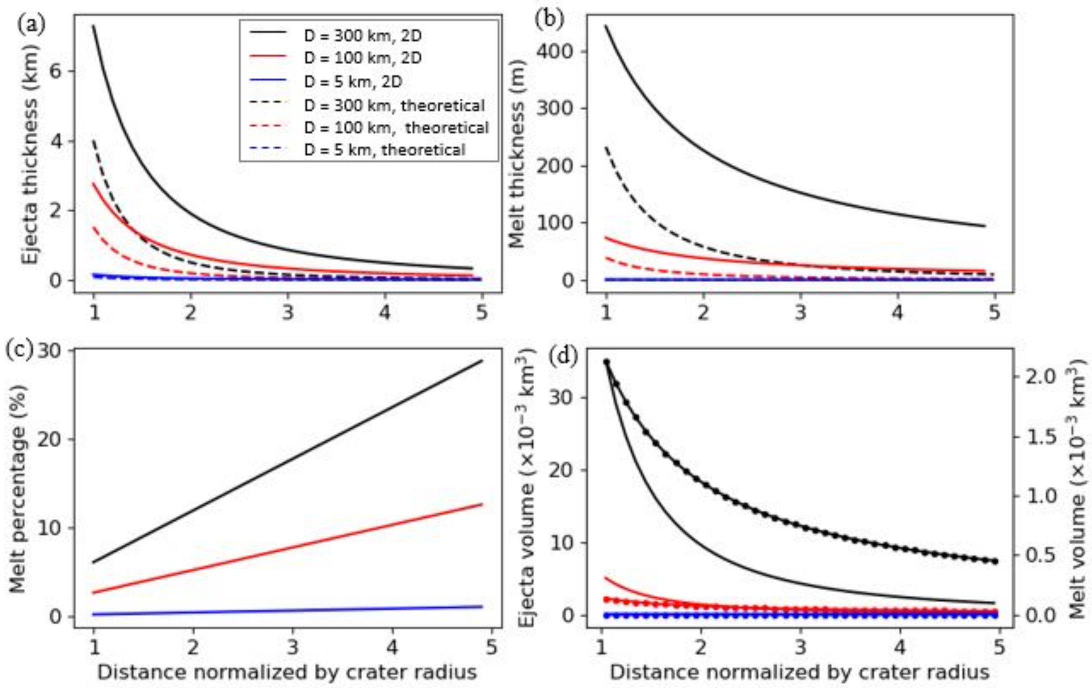

Figure 3 Distribution of ejecta and melt with increasing distance from the crater center, where black, red and blue are from craters with diameter as 300, 100, and 5 km, respectively. Dashed and solid lines are on the basis of theoretical and compressed 2D models, respectively. (a) Ejecta thickness distribution. (b) Melt thickness distribution (c) Melt percentage in ejecta. (d) Ejecta (solid lines, left *y*-axis) and melt volume (lines with dots, right *y*-axis) in a compressed 2D model taking the band width of 1 m.

2.2 Reducing the problem to two dimensions

Because of the complexity of tracking all the material during the cumulative gardening process, we reduce the problem to two dimensions (2D) in this study, so that the evolving distribution of the melt component with depth along a path is simulated. It is helpful for the analysis and understanding of simulation results and builds a bridge to a three dimensional model in future work.

To investigate the lateral diffusion of melt, a narrow band is chosen for modelling. By dividing the surface into cells, the ejecta volume and the portion of unheated and melted materials are recorded laterally and with depth, tracking the ages of the newly-generated impact melts as current model time. The cell resolution is chosen as 2 km. The diffusion of melt is well-traced at such a resolution, while saving computational expense. D_{min} is thus taken as 5 km, the D_t of which is about twice the cell resolution. Therefore, the gardening trace of smallest simulated craters can also be well-recorded. The thickness of the ejecta layer and melt is multiplied by the overlying fraction when partial coverage of a cell occurs.

Only the material deposited along the band is traced. If we were to treat the model in three dimensions, the quantity of materials in the band would decrease on each impact because material is transported outside the band (Figure 4a). However, on the real lunar surface, the total mass of material on the band would be constant in the long term with the symmetrical return of material from outside the band. To conserve the mass in 2D model, we take instead that all the excavated materials on the band are transported along the band instead of spread radially (Figure 4). In addition, although after the concentric 'compression' the ejecta thickness becomes larger, we maintain the melt fraction in the ejecta (Figure 3c), ensuring that the main characteristics of the melt distribution remain unchanged.

This procedure may be considered as compensating the ejecta produced by craters outside the band that the model does not record. In our simulations, the band width, B, is taken to be much smaller than the crater size such that the locations at the same longitudinal sites of the band have the same distance to the impact center. We can easily obtain the total volume of the excavated materials beneath the band: $V_{\mathrm{exc\_band}} = 2R_{\mathrm{t}}^2B/15$. The volume of ejected material that is deposited along the band is $V_{\mathrm{ejecta\_band}} = 2\bar{\delta}R_{ce}B$, where $\bar{\delta} = 3A/\left(25{R_t}^3\right)$ is the average ejecta thickness, and $R_{\mathrm{ce}} = 4R_{\mathrm{t}}$ is the radial length of the ejecta coverage. The lost volume after ejection is then equal to $V_{\mathrm{loss}} = 7R_{\mathrm{t}}^2B/75$. This lost material is added to the band for mass compensation. Such compensation is easy to realize for smaller craters on the lunar surface, because their high frequency of occurrence quickly leads to an average state with no net movement. For example, the lost volume of an impact with R_{t} in radius can be compensated by about $0.36R_{\mathrm{t}}/B$ occurrences of a nearby impact with the same size. For larger craters, the lower impact frequency may mean that the average state is not so quickly attained, but we assume for the sake of the 2D model that this does occur.

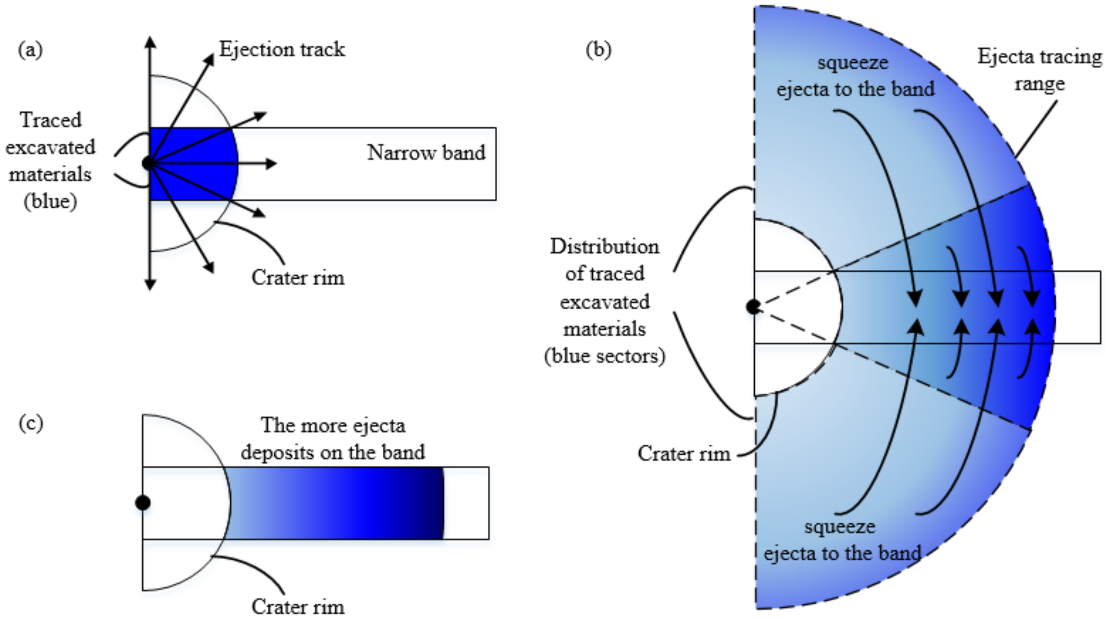

Figure 4 Schematic distribution of excavated materials for a crater half-space inside the band when reducing the problem to two dimensions. (a) The excavated material in the narrow band of the 2D model is traced (blue). This material would be radially distributed as indicated by the black arrows. (b) The excavated materials are distributed within five radii (semicircle outlined by dashed curves), where the farther locations receive less absolute melt quantity, but it nevertheless makes up a greater fraction of the ejecta there, indicated by the darker blue. To conserve the mass in 2D, the ejecta materials that would be deposited outside the band are added into it. (c) The band therefore possesses more ejecta material appearing the much darker blue. This compensates ejecta generated by craters outside the band that the model does not record, while maintaining a realistic average transport distance.

The compensation process is shown in Figure 4. As seen that the material that is distributed outside the band is compressed into it resulting in a local concentration of material shown as the deeper color in Figure 4c. Taking craters with 300, 100, and 5 km in D_t as an example, Figure 3 (solid lines) shows the distribution of ejecta and melt of craters after the concentric 'compression'. Both the ejecta and melt products are increased: the ejecta thickness is 3 km (1.3 km, 0.15 km) thicker at the crater rim, and 0.3 km (0.1 km, 0.006 km) thicker at five radii for 300-km (100-km, 5-km) crater; the melt thickness is 211 m (34 m, 0.16 m) thicker at the crater rim, and 84 m (12 m, 0.06 m) thicker at five radii for 300-km (100-km, 5-km) crater.

To investigate the transportation of melt from selected lunar basins, a great circle passing through the Imbrium, Crisium, and Serenitatis basins was chosen for modelling (Figure 5). Since here we focus on the basin melt components, the model time was started at the estimated formation time of the oldest Serenitatis basin (4.13 Ga, Table 1) instead of 4.5 Ga. Based on $N(20)$, the number of craters larger than 20 km, measured by Fassett et al. 2012, we can estimate plausible ages for these three basins (Michael et al. 2018). The ratio of $N(1)$ (the number of craters larger than 1 km) and $N(20)$ is first calculated using the PF, which is then applied to obtain the corresponding $N(1)$ values for each basin. By looking up these $N(1)$ values in the lunar chronology function (Neukum 1983), the age of Serenitatis, Crisium, and Imbrium basin are then calculated to be 4.13, 4.09, and 3.88 Ga, respectively.

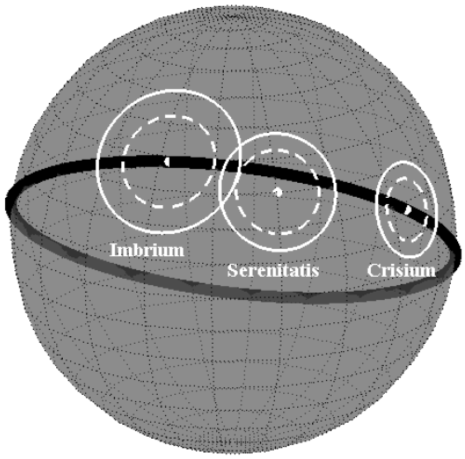

Figure 5 A band passing along the great circle through the mid- to late-forming Imbrium, Serenitatis, and Crisium basins, where the solid and dashed outlined circles indicate the rims of final and transient craters, respectively.

The number of layers in each cell becomes large as the simulation progresses, increasing the computational cost of tracing the differently aged melt (the same issue arose in the previous surface-averaged model, Michael et al. 2018). The depth in each cell is, therefore, periodically simplified into a sequence of layers where the shallower layers are thinner to preserve a fine resolution of the melt distribution near the surface, with the deeper layers having a greater thickness to maintain a more averaged distribution. The stack of layers is amalgamated into simpler ones each time the number of layers exceeds a given threshold.

3 Results

Both the size and formation rate of the simulated craters affect the distribution and volume of melt components. To better explain the model, the migration of impact melt is first explored in this section by assuming a fixed crater size with a uniform impact rate. Further simulations were performed to understand how different factors affect the presence of melt individually. Therefore, a second model was run for a size–frequency distribution that conformed to the PF but still with a uniform impact rate. Finally, we investigated the diffusion features of the melt from three mid- to late-forming basins (Serenitatis, Crisium and Imbrium basin) and carried out the complete simulation considering a realistic impact rate (Neukum, 1983) and crater size distribution (PF) . The above three simulations all use the same model with different parameters.

3.1 Migration of impact melt

How does the melt evolve laterally and with depth under the influence of subsequent impacts? Impact events cause a redistribution of material leading to migration and burial. In the first instance, we consider a series of impacts with D_t fixed at 40 km.

Figure 6 a1-a5 shows the evolving distribution of the melt from the first impact event when the 1000 km line segment experiences one, 30, 50, 100, and 150 impact events. The impact center of the first impact is set to be the midpoint of the great circle (Figure 6 a1). In Figure 6 b1-b5, we introduce the same data with a logarithmic depth scale to show more detail near the surface, noting that units of color at greater depth now represent a relatively larger volume. As seen from Figure 6 b1, when just formed, the majority of the melt stays within the crater; the remainder is ejected outside the crater where more distant locations receive a higher fraction of melt in the ejecta layer.

With an increasing number of subsequent impact events, the melt from the first impact becomes buried. As seen in Figure 6 a3 and b3, the deepest melt is located at ~7 km, after 150 impact events have occurred, which is about seven times the depth of the initial crater (~ 1 km). The buried melt can also be re-excavated to the surface exposing it to the further gardening. For example, melt buried at ~1 km depth after 30 impact events (Figure 6 b2) is re-excavated to the shallow surface leading to the abundant melt assembled between ~150 – 150 km indicated by the red regions it the top ~0.1 km in Figure 6 b3.

The later impacts spread the melt further through the ejection process. Almost all the 1000 km path segment contains at least a minor component of the first impact's melt after 150 impacts (Figure 6 a5 and b5), but the abundance varies: Figure 6 b5 indicates that the uppermost layer (top ten meters) with a melt fraction larger than 0.01 extends about 380 km around the initial concentration region (i.e., center part of the path in Figure 6 b1); more distant locations have very low concentrations (10^{-5} or less shown as grey color in Figure 6, indicating regions that have at least some admixture of melt).

The melt is also depleted through gardening because of the re-melting by later impacts. The distribution of the melt volume of the first impact is shown in Figure 6 c1-c5. Initially, there is 6.6×10^{-3} km^3 deposited over the narrow band (chosen as 1 m in width), which is ~0.003% of the total volume for a crater with D_t at 40 km (206.1 km^3). The majority of it remains inside the crater generating a pronounced peak; this peak still remains after 50 impact events. After 100 impacts have occurred, ~13% of the total melt is depleted (Figure 6 c4), and the melt that was initially deposited inside the crater has been transported over a wider range indicated by the broader flatter peak. The final 50 impacts re-melted (depleted) an additional 3% of the melt (Figure 6 c4), continuing to spread the melt distribution.

The distributions of the total generated impact melt from all the impacts are shown in Figure 6 d1-d5. More and more impact melt (from 0.007 km^3 to 0.655 km^3) is generated with the increasing number of impact events, but the local diversity is quite strong. After 150 impact events, each location is covered with at least 5×10^{-4} km^3 melt. The surface layer experiencing continual gardening accumulates melt with various ages.

To summarize, we see that the existing melt is depleted by re-melting, partially transported away from its initial location by excavation, buried more deeply by overlaying ejecta from subsequent impacts, and buried melt is sometimes re-excavated to the surface where it is subject to further gardening.

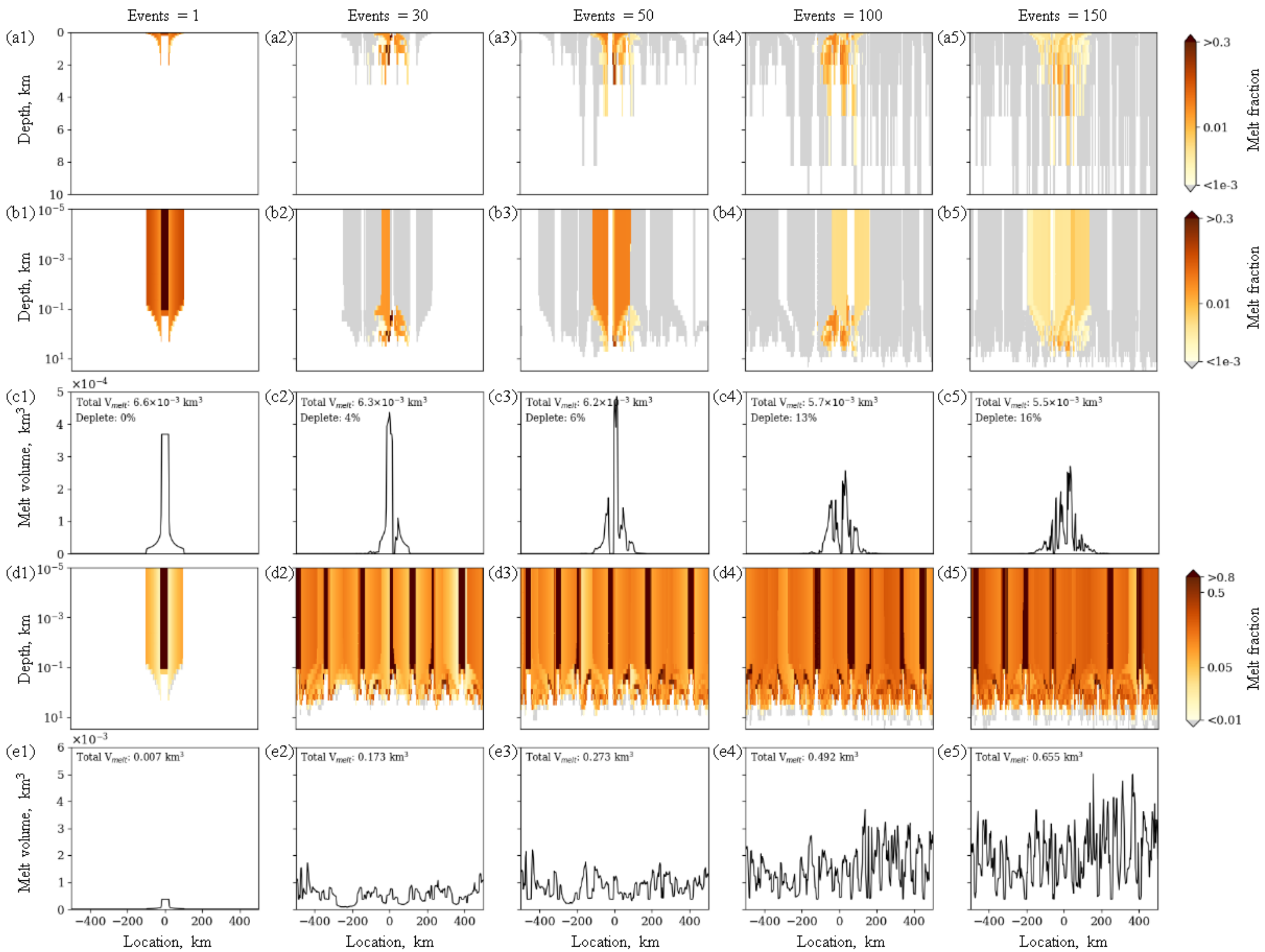

Figure 6 Evolving distribution of impact melt after one (first column), 30 (second column), 50 (third column), 100 (fourth column) and 150 (last column) impact events, where D_t is fixed to be 40 km. Both a1-a5 (linear depth) and b1-b5 (logarithmic depth) show the spatial distribution of the impact melt from the first impact event. The latter better displays the melt distribution at the near surface. The distribution of total melt volume of the first impact event (c1-c5) indicates that the generated impact melt is depleted by the re-melting process of subsequent impact events. The melt that was transported farthest has the smallest volume. The total melt volume distribution is shown in e1-e5. More and more impact melt is generated with the increasing number of impact events, but the local diversity is quite strong. In a1-a5, b1-b5, and d1-d5, depth is referenced to the surface boundary, and thus shows no topography. Note that all the calculations concerning melt volume are based on a band of 1 m in width.

3.2 Realistic crater size distribution

The situation where the SFD of craters statistically conforms to the PF and the impact rate is uniform is simulated to study the influence of crater size on impact melt distribution. The path length is chosen as 2000 km, the approximate ejecta coverage of the theoretical maximum crater diameter (i.e. D_{max}). One hundred and fifty impact events are simulated with diameters ranging from 5.1 to 247.6 km. The spatial distribution of the impact craters is shown in Figure 7a, where the different colors are applied to better distinguish the impact positions. The point size shows the scale of the impact craters, where the bigger points represent larger crater sizes. Note that the smallest craters are exaggerated to make them visible. The impact events are randomly distributed along the path. Because of the shape of the PF, there are many more small craters than large ones: there are 114 (76%) small craters with diameter smaller than 30 km, and only 3 (2%) craters larger than 150 km. The small-scaled impacts have a small gardening range and shallow gardening depth suggesting a light effect on the existing melt, which could, therefore, be considered as *local gardening*.

Emplaced melt can be depleted because of later impacts, but it can also be preserved if it remains buried. For example, Figure 7b shows the spatial distribution of melt from the 142nd impact (impact 'b'). It is located at -769 km on the path with a diameter of 50.0 km and followed by the big impact 'b_{next}' (the 150th), that occurred close to impact 'b' at -641 km on the path. The impact locations of both events are denoted by black arrows in Figure 7a. The impact 'b_{next}' is large (66.7 km). Its thick ejecta blanket covers the majority of the impact 'b' melt, and buries it to deeper than 200 m. Only the remaining unburied melt (at ~800 km on the path) is subjected to further gardening. The distribution of the melt volume of impact 'b' (Figure 7e) shows that almost all the produced melt by impact 'b' is preserved until the present day.

The melt generated by the small-scaled impacts is more easily depleted than that of larger impacts, for example the impacts 'c' and 'd' (black arrows in Figure 7a). The early impact 'c' with a diameter of 232.3 km is much bigger than the recent impact 'd' (14.8 km in diameter). The spatial distributions of the generated melt (Figure 7c and d) suggest that the melt of early impact 'c' (the 29th impact) is extensively gardened, while that of the young melt of impact 'd' (the 118th impact) experiences less gardening.

However, as seen from the distribution of melt volume, only 6.5% of the total generated melt of impact ‘c’ is depleted until the present day (Figure 7f). In contrast, the melt of the recent small impact ‘d’ decreases by 24.8% (Figure 7g).

To summarize, the small-scaled impacts garden the surface within a narrow range at shallow depth, which may be characterized as *local gardening*. The fate of the impact melt not only depends on the age, but also the burial depth that may protect it from further gardening. Furthermore, large-scale impacts generate a greater volume of melt, a considerable fraction of which is expected to survive to the present day; the melt from small impacts, however, is much more easily transported and diminished.

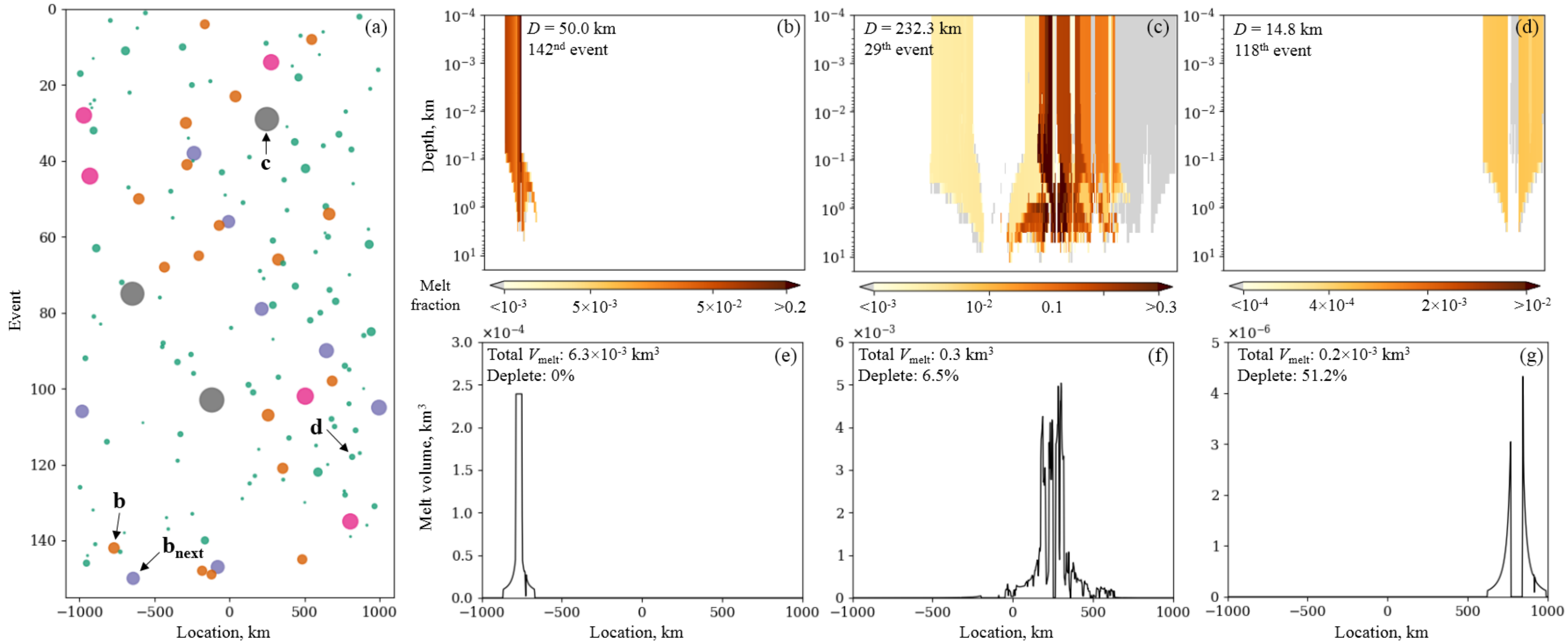

Figure 7 (a) Spatial distribution of impact craters, where bigger points represent the larger impact craters (but not to scale), and different colors are applied to better distinguish the impact positions. (b), (c), and (d) show the spatial distribution of melt from impact ‘b’, ‘c’, and ‘d’, respectively, the impact location of which is denoted by the arrows in (a). b_{next} in (a) points out the location of the impact that occurred after impact ‘b’. The distribution of melt volume of impact ‘b’, ‘c’, and ‘d’ is shown in (e), (f), and (g), respectively. Note that all the calculations concerning melt volume are based on a chosen band width of 1 m.

3.3 Diffusion of basin melt

Because of the exponential increase of the melt volume with increasing crater size (Figure 3), giant basin-forming events produce an overwhelmingly greater volume of melt than smaller impacts with the ejecta covering a much wider area and a thicker melt lens. Because of the importance of the identification of basin melt to the lunar chronology system and thus to our understanding of lunar geological history, the migration of basin material through impacts is of special interest.

The evolving distribution of melt from basin-forming events was simulated in a third model run where the impact rate matches the CF and the crater SFD statistically conforms to the PF (Neukum, 1983). The mid- to late-forming Serenitatis, Crisium, and Imbrium basins were chosen for modeling. Their great size results in an extensive gardening range and the generated melt is very likely to survive in the near surface due to their relatively late occurrence. It should be noted that since the relationship between D and D_t mentioned in section 2.1 cannot be extrapolated to the basin size (e.g., Melosh et al. 2017), the D_t values of basins in this study adopt the results from Wieczorek & Phillips (1999) where the diameter of excavation cavities is obtained by using a crustal thickness model (Table 1). D and D_t of basins are shown in Figure 5 (Table 1). We chose a great circle which passes through these three basins (Figure 5), and the center of Imbrium basin is set as the midpoint of the circle. The path length is 10920 km, the circumference of the Moon.

Table 1 Model age, size, and location of the three basins in simulation

Basin	***N*(20)**[1]	***N*(20)e**[1]	**Age (Ga)**[2]	**D_t (km)**[3]	***d* (km)**[4]
Serenitatis	155	60	4.13	657 (582)[5]	865
Crisium	113	11	4.09	487	2049
Imbrium	30	5	3.88	744	0

[1] Fassett et al. 2012; [2] Spudis 1993; [2] The plausible ages of basins are estimated based on *N*(20) from Fassett et al. 2012; [3] Wieczorek & Phillips 1999; [4] Distance from Imbrium basin center;[5] (582 km) is the length that Serenitatis basin cross the great circle.

The traditional tail-end impact rate (i.e. the impact flux declines exponentially over the first billion years of lunar history) is applied in this simulation (Figure 8a, Neukum, 1983). The number of impacts occurring along the path is calculated as the square root of the number of impacts that would theoretically occur in a flat square area with edge length equal to the path length. Including the three basin events, we simulate 390 impacts that occur along the band. It can be seen in Figure 8a that the impact rate before ~3.0 Ga is much higher than that in the later period: 347 (89%) events occur between 3.80 and 4.13 Ga; 38 (10%) events happen between 3.0 and 3.8 Ga; only 5 (1%) during the last 3.0 Ga. As before, the small impacts predominate: 293 (75%) craters with diameter smaller than 30 km, and only 11 (3%) craters larger than 150 km. The distribution of impact locations is shown in Figure 8b. To better distinguish the early dense impacts, only those which occur before 3.6 Ga are shown. The three basin events are indicated with arrows.

We assume that 75% of the melt from Serenitatis, Crisium, and Imbrium basin is retained within each cavity, generating the 31, 18, and 39 km thick melt lens, respectively. The ejecta range is 2910, 2435, and 3720 km, respectively, much greater than for the smaller craters in the above simulations. Those impacts are so small compared with the basin-forming events that the mixing could be considered as *local gardening*.

The present-day distribution of impact melt with depth for three basins is shown in Figure 8c-e. The initially generated melt is depleted and redistributed by the subsequent impact events: the smaller impacts mainly locally garden the near-surface materials, but the giant basin-forming events can significantly alter the existing basin melt reservoirs. As can be seen, Serenitatis melt in the near surface is almost non-existent with a melt fraction smaller than ~0.005. Some of it is even smaller than 0.001 denoted by the grey color in Figure 8c, the west and east part of which is mainly re-distributed by the subsequent Imbrium and Crisium event, respectively. The ejecta materials from both Crisium and Imbrium basins cover the remaining melt of Serenitatis basin burying its melt to a greater depth. Some of the buried melt was re-excavated to the surface where it was subject to further gardening, such as the melt at ~400 km along the path (arrow in Figure 8c). The Crisium basin melt at the near surface is also significantly depleted and irregularly distributed, where the ejecta in the west is buried by Imbrium ejecta, and the eastern part is mainly gardened by smaller impacts. Without the excavation by other basin events, most of the Crisium melt still lies around the impact center, with only a few relatively large cratering events bringing a portion of it to the surface, like the melt at ~1300 km on the path (arrow in Figure 8d). The relatively young Imbrium cavity melt distribution was not dramatically altered although several depleted patches appear in its ejecta blanket. The subsequent smaller impacts producing less melt and smaller ejecta blankets only depleted and buried a small part of the Imbrium melt, so that the Imbrium melt is still abundantly distributed in the near surface.

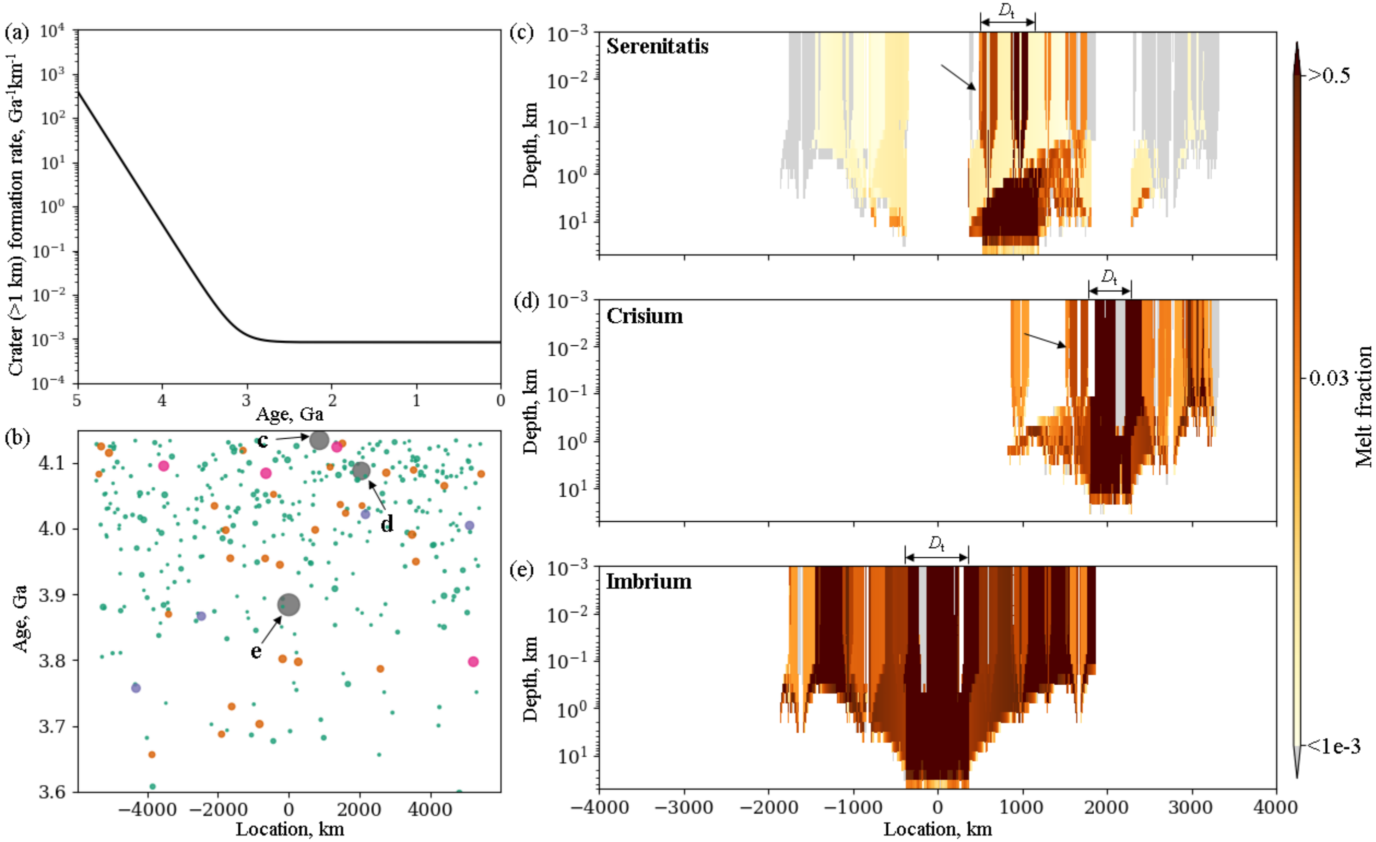

Figure 8 (a) Exponential decay rate function for crater size-frequency over time (Neukum 1983). (b) Spatial distribution of impact centers. The locations of Imbrium, Crisium, and Imbrium basin are denoted by the arrows. (c) to (e) show the present day distribution of impact melt of Serenitatis, Crisium, and Imbrium basin, respectively. The D_t of each basin is marked on top of each figure. Depth is referenced to surface boundary, and thus shows no topography. The arrows in (c) and (e) denote the re-excavated Serenitatis and Crisium melt, respectively.

The distribution of average melt fraction with depth is shown in Figure 9a where the melt of Imbrium, Crisium, and Serenitatis basins is shown in blue, green, and red, respectively. As seen that the largest and relatively young Imbrium melt remains dominant; the burial of Imbrium and Crisium ejecta blanket results in the least Serenitatis melt at the shallow ~1 km depth. The majority of Serenitatis melt is deposited at greater depths with a comparable fraction of Imbrium melt. In addition, after the formation of the Imbrium basin, the last giant impact event, the average contribution of the three basins to melt in the near surface was confirmed. The subsequent smaller craters can only diminish a small part of basin melt, and thus the average presence of basin melt is almost unchanged in the near surface shown as flat curves in Figure 9a.

The lateral distribution of melt volume is shown in Figure 9b. Because abundant melt stored within their cavities, the giant basin-forming events leave a clear signature on present day as denoted by the arrows in Figure 9b. The lesser-scaled gardening makes the distribution of the basin melt patchy. In addition, smaller impacts with diverse size randomly garden the surface producing various amounts of melt along the great circle leading to the fluctuations in Figure 9b. This makes it difficult to estimate the fraction of basin melt at specific sites, such as Apollo and Luna sampling sites, because every instance of the random bombardment in the model will produce a statistically different outcome.

The distribution of the differently-aged melt (Figure 9c) also reflects the overwhelmingly large quantity of basin melt (three prominent peaks indicated by arrows). In addition, the earlier more intense bombardment results in the higher abundance of melt older than 3.5 Ga. The recent lower impact rate generates much less melt, but the majority of it could survive until the present day because of the small probability of being gardened.

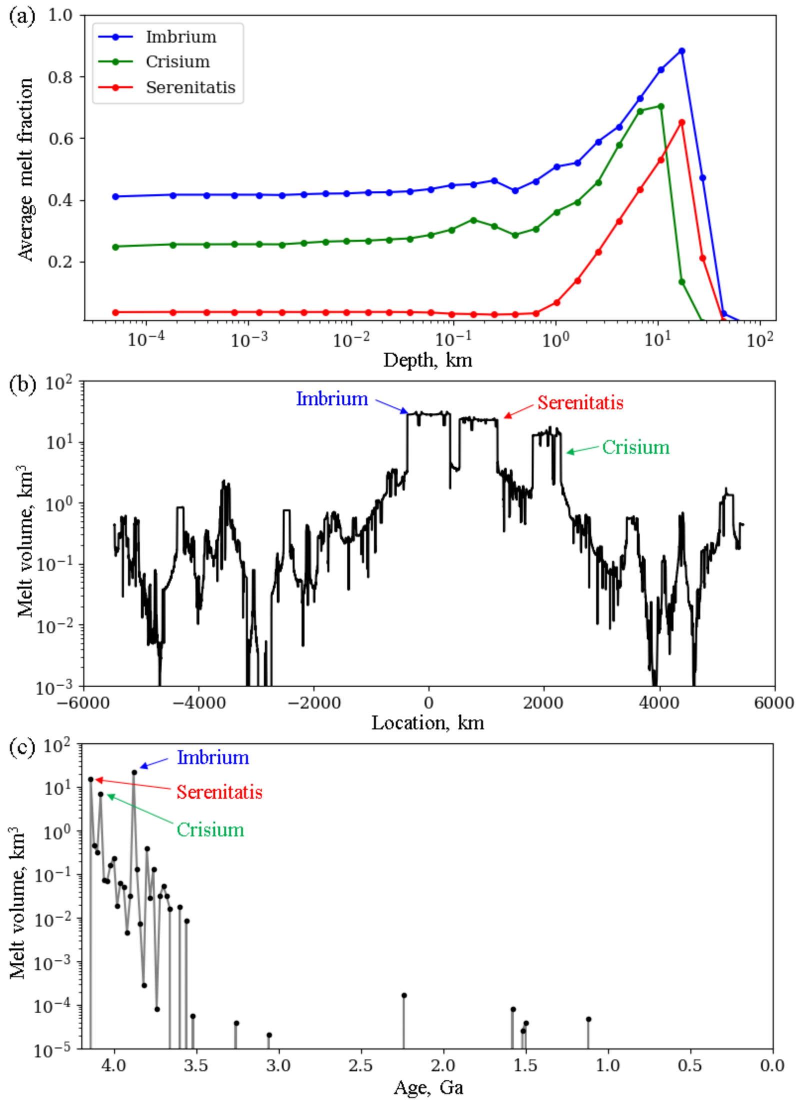

Figure 9 (a) The distributions of melt fraction with depth, where the red, green, and blue indicate the melt from Serenitatis, Crisium, and Imbrium basins, respectively. The dots on curves indicate the thickness of the simplified stack layers. (b) The local distribution of melt volume. The arrows point out the peak values caused by the three basins. (c) The distributions of melt volume with age. The arrows point out the melt generated by the three basins. Note that all the calculations concerning melt volume are based on a chosen band width of 1 m.

4 Discussion

4.1 Characteristics of basin melt diffusion

Lunar highland rocks contain evidence (e.g., K-Ar system) of impact events on an ancient lunar curst, through which geochemists are able to trace the early lunar bombardment history. Tera et al. (1974) found the clustering of radiometric dates around 3.9–4.0 Ga based on the lunar highland samples, the cause of which has been debated for decades (e.g., Baldwin 1974; Bottke et al. 2012; Chapman et al. 2007; Cohen 2000; Hartmann 2003; Morbidelli et al. 2012). Tera et al. (1974) suggested that it resulted from an intense bombardment episode on the Moon, called the terminal cataclysm. Michael et al. 2018 investigated whether or not a lunar terminal cataclysm occurred by reanalyzing the radiometric dating of lunar highland rocks and building a numerical surface-averaged impact gardening model. Their simulation results suggested that the cataclysm, if it occurred, should generate a rather intensive peak, which is inconsistent with the relative plot of summarized radiometric ages. The clustered ages were more likely caused by the contamination of Imbrium ejecta at the sampling sites. The results on transportation and mixing of basin melt obtained in this study are intended to further refine our understanding of how this process might occur.

Impact melt is laterally transported away from its source if there are sufficient later impacts as described in section 3.1. The melt from small impacts, with relatively small volume, is easily depleted before it is transported very far. In contrast, the large quantity of melt generated by large impacts, especially that of the giant basin events, can migrate significant distances. Figure 10a-c shows the averaged fraction (sum of the average melt fraction of each layer that is weighted by the ratio of its layer thickness to the total depth) of melt from Serenitatis, Crisium, and Imbrium basin, respectively, in the near surface along the great circle defining the modeled area. The thinner surface layer, where Apollo and Luna samples were collected and the *in situ* drill tube experiments were performed (McKay et al. 1991; Vaniman et al. 1991), is chosen to investigate the scenario of the melt distribution. The collected samples in the topmost surface have been subjected to extensive impact gardening. The melt distribution range of Serenitatis basin is about two times larger than its initial state because of the re-excavation by the subsequent Crisium and Imbrium basin events (Figure 8). Without transportation by the giant basin events, the melt distribution range of both the Crisium and Imbrium basins, nevertheless, has not been significantly altered. This suggests that local gardening by smaller impacts is not able to spread a significant part of the basin melt to more distant locations, although it can result in a local enrichment zone in the surface fine layer if the basin melt is freshly excavated. The lateral transportation efficiency of the impact melt by smaller impacts is, therefore, not high if only the proximal ejecta process (five radii in this study) is considered. Studies on the mixing zone at mare/highland contacts also support the low transportation efficiency of surficial materials, where the narrow mixing area has been interpreted as the result of the local mixing (continuous ejecta) rather than distal ejecta deposition (e.g., Huang et al. 2017; Li & Mustard 2005; Li & Mustard 2000). The melt materials in the distal ejecta, that our model did not trace, may indeed be transported very far, but their fraction is small (usually <15% of the total ejecta material). In addition, it is heterogeneously distributed. The majority of distal ejecta is concentrated in patchy rays which can be easily observed through high-resolution images if it is young. This has helped to find plausible source of distal materials in the collected samples. For example, the abundant highland materials of Apollo 15 samples were thought to be correlated with Aristillus and Autolycus craters based on their bright ray trace (Carr et al., 1971; LSPET, 1972; Spudis and Ryder, 1985).

Looking at the distribution with depth, existing impact melt can both be buried to greater depth and/or re-excavated to the near surface as described in section 3.1. As seen from Figure 8, the local gardening by the smaller impact events after the formation of basins strongly mixed the basin melt in the surface layers resulting in an irregular distribution which has significant consequences for scooped samples at the landing sites. For the younger Imbrium basin, the melt is depleted by local gardening. For an older basin like Serenitatis, the distribution is more complicated, because the majority of the melt is deeply buried by the subsequent Imbrium and Crisium basin events. When subsequent lesser-scaled impacts are big enough, a portion of the buried melt could be re-excavated to the surface, augmenting the local melt fraction and generating an enrichment zone like the area at ~400 km in Figure 8c and ~1300 km in Figure 8d. In addition, the melt at deep depth, where the smaller impacts are not able to excavate, is shielded from the gardening process.

4.2 Comparison with radiometric dating

In general, the remaining basin melt at the present day is distributed in/around the center of the impact. As seen from Figure 8, the majority of basin melt is distributed inside the original cavities. Although the old Serenitatis melt is buried, local gardening within the basin still has a high probability of excavating the melt beneath, resulting in a melt enrichment zone. For the melt in the ejecta, the low lateral transportation efficiency (described in section 254.1) protects it from long-distance migration. Basin melt is, therefore, spread within proximal range if no basin-scaled gardening occurs.

The small distance between the basins and the sampling sites (Apollo 14-17 and Luna 20) provided a high probability of finding components of basin melt in the collected samples. The arrows in Figure 10a-c point out the relative positions between the sampling sites and the center of each basin (each sampling site has two probable values of melt fraction indicated by arrows, because there are two sites on the path that have the same distance to a particular location). Our simulation results show that the materials collected at the Apollo and Luna sampling locations could contain the basin melt to different degrees, where the older basin generally remains the least abundant melt in the surficial layer: Imbrium melt could be expected at Apollo 14-17 sampling sites with a fraction of about 0.6, 0.3, 0.5 and 0.4, respectively; Crisium melt would be expected at Luna 20 and Apollo 17 sampling sites with a similar fraction about 0.05; and Serenitatis melt would be present at all the Apollo and Luna sampling sites but the less abundance where the fraction is about 0.002, 0.018, 0.00, 0.018, and 0.0016 for Apollo 14-17 and Luna 20 sampling sites, respectively.

To compare with the radiometric age results, Figure 10d presents the relative age probability plots for K-Ar ages of highland rock from Apollo and Luna samples from the data of Michael et al. (2018). There are 25, 8, 41, 36 and 7 determinations of impact melt breccias for Apollo 14, 15, 16, and Lunar 20 highland samples, respectively: the Apollo 14 plot shows a prominent bulge centered at ~3.85 Ga with four secondary peaks at 3.80, 3.85, 3.89, and 3.95 Ga and one additional minor peak at 4.10 Ga; the Apollo 15 plot shows only one peak at 3.87 Ga; the Apollo 16 plot shows one prominent peak at 3.87 Ga with three additional peaks at 3.67, 3.89 and 4.20 Ga; the Apollo 17 plot shows a prominent peak at 3.88 Ga with three smaller peaks at 3.98, 4.05, and 4.13 Ga; Luna 20 plot shows four comparable small peaks at 3.75, 3.88, 3.98 and 4.10 Ga. The small number of age determinations suggests the secondary peaks may be within the statistical noise and the most meaningful feature is probably the prominent bulge.

The prominent peak around 3.88 Ga seen in the Apollo samples is consistent with the simulated results that predict a high fraction of Imbrium melt at these sites. For Crisium melt, only Apollo 17 and Luna 20 sampling sites are located in its ejecta range, and the others are too far to mix with its melt. Figure 10d shows that there is no obvious peak around 4.09 Ga from the Luna

20 and Apollo 17 samples, but both sites are very likely to collect samples in this age with the relative probability of ~0.2 and ~0.5, respectively. It is consistent with the predicted smaller fraction of Crisium melt comparing with predicted abundant Imbrium melt described above. Therefore, if the basin ages used in this study are close to the true values, the distribution of radiometric ages could be a consequence of the mixing of basin melt. For Serenitatis melt, the radiometric ages differ from the simulated results in that we expect very little to no Serenitatis melt in the near-surface. The radiometric results show no presence of a peak at 4.13 Ga at the Apollo 14 and 15 sampling sites. However, one small peak around 4.13 Ga is seen in the Apollo 17 radiometric sample ages. Since the majority of Serenitatis melt is buried to greater depth by the Imbrium and Crisium basin events, its distribution in the near-surface layer depends on the gardening by smaller impacts that could re-excavated buried Serenitatis melt, if big enough, forming local melt-enriched zones. Nevertheless, the occurrence locations of smaller impacts are random such that a single simulation will not necessarily match the real abundances at any specific site. That is to say, the predicted melt abundance for the older basins in the shallow surface has lower accuracy. In addition, the heavy gardening that the Serenitatis melt has suffered since formation may have pulverized the melt materials to such a fine grain size that it has not been possible to identify its age with the current radiometric techniques.

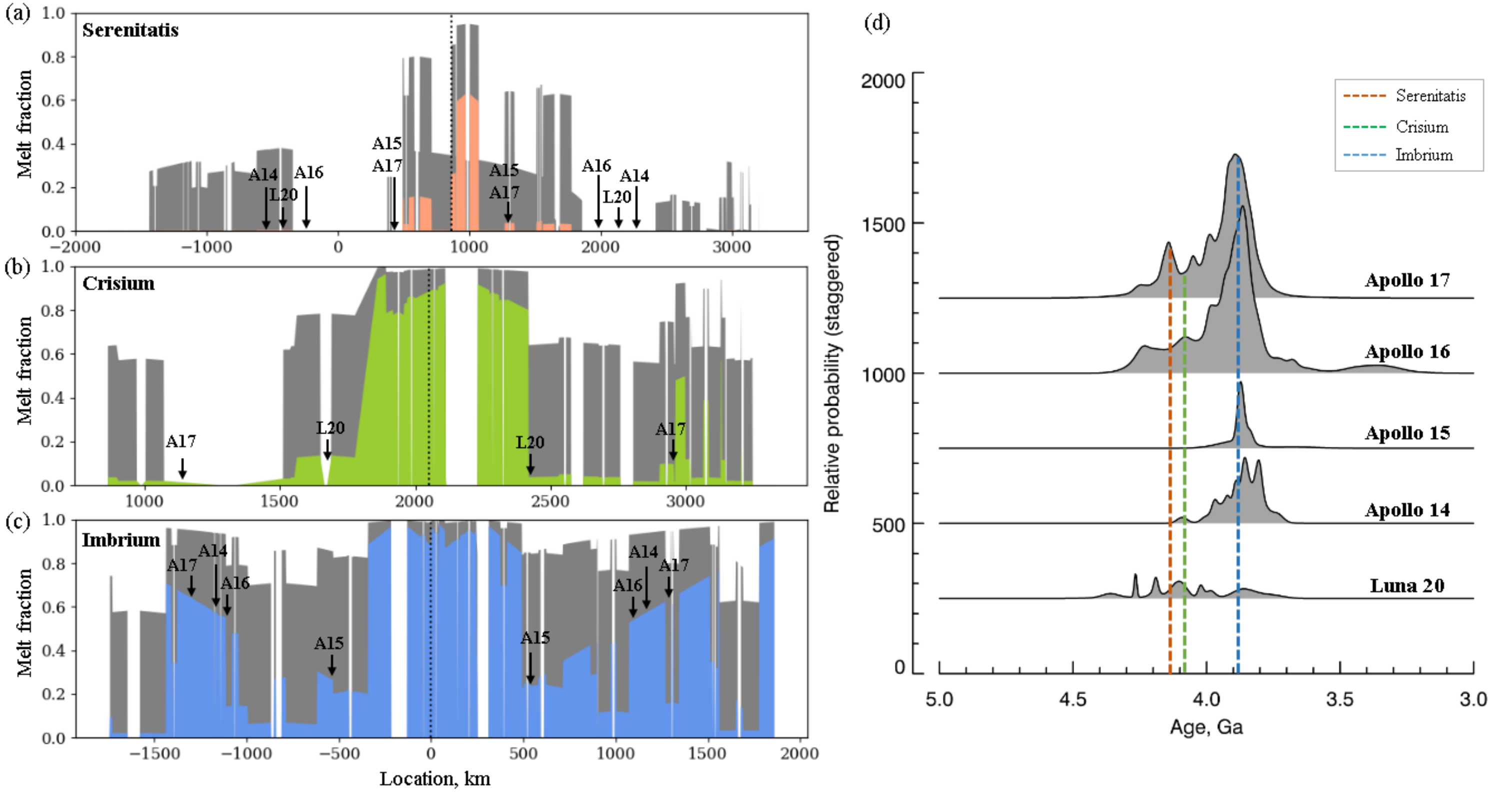

Figure 10 Average fraction of melt from Serenitatis basin (a), Crisium basin (b), and Imbrium basin (c) in the top 0.1 m (the first stack layer). The black dashed lines indicate the center of each basin. The figures are plotted twice: the red, green, and blue shaded plots are Serenitatis, Crisium, and Imbrium melt in linear scale; the grey shaded plots are the same data in logarithmic scale to show the small values. The arrows in (a) to (c) point out the relative distances between the Apollo and Luna sampling sites and the center of each basin, where 'A' and 'L' mean 'Apollo' and 'Luna', respectively. (d) Relative age probability plots of the K-Ar ages of lunar highland rocks for the Apollo and Luna returned samples, where Apollo 14, 15, 16, and Lunar 20 highland samples have 25, 8, 41, 36 and 7 determinations, respectively (after Michael et al. 2018). The red, green, and blue dashed lines indicate the calculated possible formation times of Serenitatis (4.13 Ga), Crisium (4.09 Ga), and Imbrium (3.88 Ga) basins, respectively.

4.3 Implications for the choice of future sampling sites

Basin impact melt, that tells us about the process of giant basin-forming events and the formation time of basins (Spudis & Sliz 2017), is a prime target for future robotic or human sample return missions (Cohen et al. 2018; Ryder et al. 1989). If melt materials of more certain basin origin (like a basin melt sheet) were sampled, the age could provide a strong calibration point for the lunar chronology system (van der Bogert et al. 2018). It is thus a critical objective for lunar exploration.

Both the relative position to a basin center and the scooping depth of a sample influence the expected melt volume abundance. Figure 8 suggests that the area within or around the basin center provides the greatest probability of survival of basin melt. Without a strong disturbance by subsequent basin-scaled gardening, abundant basin melt could be collected in the surficial regolith layer (the average thickness is 5 – 6 m in the maria regions; 10 – 15 m in the highlands regions; e.g., Fa & Jin 2010; Fa et al. 2014; McKay et al. 1991; Shkuratov 2001). Nevertheless, scooped samples from the surficial layer are affected by the local smaller impact events. For the abundant young basin melt, local gardening decreases the content. In contrast, for more scarce older basin melt, local gardening may produce some enriched zones. Extended gardening in the topmost surface may also pulverize the melt materials resulting in a fragment size too small to perform radiometric dating for current radiometric dating techniques. In addition, the melt sheet that originally covered the entire basin floor is often buried beneath extensive mare basalt that was not considered in this study, although some residue might be patchily exposed near the topographically-high mare-highland boundary of basin interior (Spudis & Sliz 2017). All the above point towards the low probability of collecting old basin melt from the shallow surface.

Pure basin melt has a larger probability of being present at greater depths within basins as shown in Figure 8. We may expect that higher melt abundances could be sampled from low-lying outcrops within a basin, such as on the degraded walls of later-forming craters. Y.-H. Huang et al. (2018) also suggests a deeper sampling depth by building a model to investigate the gardening process of lunar glass spherules, one of the melt products. They suggest that a shallow surface sample is more likely to yield young melt, and the old melt materials in the topmost layer could be much diluted by younger deposits, while shielding them at greater depth.

The Chinese CE-4 mission this year will explore the SPA basin. The U.S. National Research

Council (2007) identified that CE-4 mission can address the existence of the SPA melt (J. Huang et al. 2018; Wu et al. 2017), considered the oldest on the Moon (Petro & Pieters 2004). The melt materials could, therefore, have been buried and depleted by the subsequent impact events, especially in the shallow surface available for sampling. The aim should be to explore material from as deep as possible where the buried SPA melt could be have been shielded from intensive gardening: such materials might be found in the low-lying outcrops or near the rim of a later-formed nearby big impact crater, like Apollo basin and Von Kármán crater (J. Huang et al. 2018; Ivanov et al. 2018): the selected potential landing sites, where SPA melt material was likely re-excavated during formation.

4.4 Other potential factors affecting the melt distribution

Impact angle: Previous analytical studies found the relationship between the volume of generated impact melt and the crater diameter used in this study: $V_{\mathrm{melt}} = cD_t^{d}$ (Ahrens & O'Keefe 1977; Cintala & Grieve 1998; Maher 1988; Pierazzo et al. 1997). Nevertheless, these results were based on the assumption of a vertical impact trajectory. With the development of computer performance, three-dimensional numerical simulations have been run to investigate the effect of the impact angle. Using hydrocode modeling, Pierazzo & Melosh (2000) found that more impact melt is generated with increasing impact angle (angle between the surface and impact trajectory). Abramov et al. 2012, making use of classic impact experiments, analytical studies, and numerical hydrocode simulations suggest that the volume of impact melt produced by a vertical impact is ~1.6 times more than that from the most probable oblique impact (45°) on the Moon. However, as described in section 3.1, excavation and burial play more important roles in melt diffusion by dominating the transportation range and deposition depth. The probable over-estimated melt volume would not significantly change the features of the melt diffusion, although it could change the absolute abundances.

Scaling of crater diameter: There are various scaling laws for D and D_t especially for complex craters, because of the collapse of transient craters during modification stage and hence the indirect measurement of transient crater size (Melosh 1989). For example, based on observations of ejecta at terrestrial and lunar craters, Croft (1985) derived an empirical relationship of $(D/D_t) = (D/D_Q)^{0.15}$. By combining a geometric model with the model of Holsapple (1993), Krüger et al. (2017) concluded that $D_t = 0.2799D^{1.1}$. Thus, different crater sizes are obtained using different scaling laws, leading to the difference in calculated melt production.

The calculation of the basin melt uses the same scaling laws as for smaller impacts in this study. However, the formation of giant basin events is more complicated, and these scaling laws might not be validly extrapolated to the basin size. Firstly, the hotter Moon during the formation of basins provides the higher internal energy resulting in the more abundant of generated melt (Abramov et al. 2012; Zhu et al. 2017). In addition, it was found that the giant impacts are affected by the target body's surface curvature, and the produced melt has no clear relationship with the basin size (Schultz and Crawford 2016). Furthermore, the terrains (i.e. multi-rings) formed during the late modification stage of cratering make the melt spatial distribution more complicated. The present day distribution of the melt from basins obtained in this study thus likely represents a lower limit.

The transient cavity size of basins remains poorly understood because of their complicated formation conditions and great scale. In this study, we use the measurements of Wieczorek and Phillips (1999) to obtain the total melt volume of basins. However, there have been diverse estimates of transient cavities of lunar basins (Hikida & Wieczorek 2007; Potter et al. 2012; Potts & von Frese 2003). For example, Hikida and Wieczorek (2007) estimated the excavation cavity diameters of 718, 560, and 895 km for Serenitatis, Crisium and Imbrium basins, respectively, which are 10%–20% larger than values used here. The corresponding volumes of melts are thus 1.4–2.0 times larger than values used in the paper. To figure out the potential bias caused by the measurements of basins' D_t, we tried simulations with 1.5 times greater size of basin transient diameter. The greater size results in a larger ejecta coverage and a thicker melt lens within basins, but the overall pattern of basin melt diffusion is similar to that in Figure 8c-e.

Emplacement of ejecta: On the real lunar surface, the ejected materials would mix with local materials during emplacement. This results in a lower fraction of newly-generated melt at shallow depths, because otherwise more deeply-seated materials would be excavated to the surface. However, the overall picture of the pattern of evolving melt would not change. In order not to make model overly difficult to follow, we did not include this local mixing process in this work. We take the impact melt to form as a simple disc-like lens in a crater, which is a simplification. More realistically, we expect some of the hotter material to penetrate and mix into the fragmented material beneath the crater floor.

5 Conclusions

We investigate the mixing behavior of impact melt that is exposed to cumulative impact gardening. Once formed, the melt could be depleted by re-melting, spread to more distant locations by excavation, and buried by the overlaying ejecta of subsequent impacts. Large-scaled impacts producing significant volume of melt may easily leave a trace in the near-surface material until the present day. High-frequency smaller impacts, the melt of which is more easily depleted, change the local melt component in the near-surface.

To investigate the evolving distribution of the melt from giant basin events, three mid- to late-forming basins, namely Serenitatis, Crisium, and Imbrium basins were chosen for modeling. Plausible ages for the three basins were calculated to be 4.13, 4.09, and 3.88 Ga, respectively. There is abundant melt of the relatively young Imbrium and Crisium in the near surface, but local gardening by smaller impacts regionally diminishes the melt abundance; there is less Serenitatis melt in the near surface because of the burial of Imbrium and Crisium ejecta, but later impact events may build local melt-enriched zones by re-excavating the underlying melt.

The survival probability of basin melt at the Apollo and Luna sampling sites is quantitatively assessed in this study. The relatively young Imbrium melt might be abundant at Apollo 14-17 sampling sites with a fraction ranging from 0.3 to 0.6; Crisium melt could be found at Luna 20 and Apollo 17 sampling sites with a similar fraction about 0.05, each. The relatively old Serenitatis melt was exposed to heavy subsequent gardening, and its abundance should be much less or zero at these sampling sites. The observed prominent peak around 3.88 Ga, the lower values around 4.09 Ga, and the general absence around 4.13 Ga in the K-Ar isotopic ages from Apollo and Luna highland samples are consistent with our simulation results. We may therefore conclude that, particularly for the case of Imbrium, the clustered radiometric ages around 3.9–4.0 Ga for Apollo and Luna highland samples supports a sample bias, rather than the cataclysm scenario.

Our simulation results may be applied to predict the expected sampling of differently-aged melt in future sampling work. The area within a basin should possess a high fraction of basin melt, particularly for younger basins. The shallow surface might originally have abundant basin melt, but it could be strongly affected by the local impacts, buried by mare flooding, and diluted by younger melt. Besides, the pulverized materials with fine grain size may be difficult to date using the current radiometric techniques. Pure basin melt is expected at greater depths within basins, which may be re-excavated by the more recent large impacts. This year's Chinese CE-

4 mission that will land on lunar farside with a rover, should preferentially investigate deep-lying material. SPA melt might be found on the low-lying outcrops or near the rim of a later-formed large impact crater within a basin, such as Apollo or Von Kármán.

In the future, we intend to extend the model to consider ejecta movement in three dimensions to obtain a better view of the coverage and the abundance of basin melt in the present day. The abundance of differently-aged melt at some specific locations, especially sampling sites, is expected to be better estimated. It is expected to find new constraints on the impact rate function, and hence improve our understanding of the lunar bombardment history.

Acknowledgements: We gratefully acknowledge Carolyn van der Bogert and Tomokatsu Morota for their careful reviews of the manuscript and discussions with Alexander Basilevsky, Menghua Zhu, Robert Luther, Csilla Orgel and Natalia Artemieva. This work was supported by German Research Foundation (DFG) SFB TRR-170-1 TP A4. This is TRR-170 contribution 57.

References

Abramov, O., Wong, S.M. & Kring, D.A., 2012. Differential melt scaling for oblique impacts on terrestrial planets. *Icarus*, 218(2), pp.906–916.

Ahrens, T.J. & O’Keefe, J.D., 1977. Equations of state and impact-induced shock-wave attenuation on the moon. In *Impact and Explosion Cratering*. pp. 639–656.

Baldwin, R.B., 1974. Was there a “terminal lunar cataclysm” 3.9-4.0×109 years ago? *Icarus*, 23(2), pp.157–166.

Carr, M. H., Howard, K. A., & El-Baz, F., 1971, Geologic maps of the Apennine-Hadley region of the Moon, map 1-72, U.S. Geol. Surv. Washington, D. C.

Bottke, W.F. et al., 2012. An Archaean heavy bombardment from a destabilized extension of the asteroid belt. *Nature*, 485(7396), pp.78–81.

Chapman, C.R., Cohen, B.A. & Grinspoon, D.H., 2007. What are the real constraints on the existence and magnitude of the late heavy bombardment? *Icarus*, 189(1), pp.233–245.

Cintala, M.J. & Grieve, R.A.F., 1998. Scaling impact melting and crater dimensions: Implications for the lunar cratering record. *Meteoritics and Planetary Science*, 33(4), pp.889–912.

Cohen, B.A., 2000. Support for the Lunar Cataclysm Hypothesis from Lunar Meteorite Impact Melt Ages. *Science*, 290(5497), pp.1754–1756.

Cohen, B.A. et al., 2018. Curie: Constraining Solar System Bombardment Using In Situ Radiometric Dating. In: 49th Lunar and Planetary Science Conference, The Woodlands, Houston, Texas, USA.

Croft, S.K., 1985. The scaling of complex craters. *Journal of Geophysical Research Supplement*, 90(S02), pp.C828–C842.

Fa, W. et al., 2014. Regolith thickness over Sinus Iridum: Results from morphology and size-frequency distribution of small impact craters. *Journal of Geophysical Research: Planets*, 119(8), pp.1914–1935.

Fa, W. & Jin, Y.Q., 2010. A primary analysis of microwave brightness temperature of lunar surface from Chang-E 1 multi-channel radiometer observation and inversion of regolith layer thickness. *Icarus*, 207(2), pp.605–615.

Fassett, C.I. et al., 2012. Lunar impact basins: Stratigraphy, sequence and ages from superposed impact crater populations measured from Lunar Orbiter Laser Altimeter (LOLA) data. *Journal of Geophysical Research: Planets*, 117(2), pp.1–13.

Flude, S. et al., 2014. Observation of centimetre-scale argon diffusion in alkali feldspars: implications for 40Ar/39Ar thermochronology. *Geological Society, London, Special Publications*, 378(1), pp.265–275.

French, B.M., 1998. Traces of Catastrophe: A handbook of shock metamorfic effects in terrestial meteorite impact structure. *Technical Report, LPI-Contrib-954*, (954), p.120.

Hartmann, W.K., 1970. Lunar cratering chronology. *Icarus*, 13(2), pp.299–301.

Hartmann, W.K., 2003. Megaregolith evolution and cratering cataclysm models—Lunar cataclysm as a misconception (28 years later). *Meteoritics & Planetary Science*, 38(4), pp.579–593.

Haskin, L.A. et al., 1998. The case for an Imbrium origin of the Apollo thorium-rich impact-melt breccias. *Meteoritics and Planetary Science*, 33(5), pp.959–975.

Hikida, H. & Wieczorek, M.A., 2007. Crustal thickness of the Moon: New constraints from gravity inversions using polyhedral shape models. *Icarus*, 192(1), pp.150–166.

Holsapple, K.A., 1993. The scaling of impact processes in planetary sciences. *Annual review of earth and planetary sciences*, 21(1), pp.333–373.

Hörz, F. et al., 1991. Lunar surface processes. *Lunar sourcebook*, pp.61–120.

Hörz, F., Ostertag, R. & Rainey, D.A., 1983. Bunte Breccia of the Ries: Continuous deposits of large impact craters. *Reviews of Geophysics*, 21(8), pp.1667–1725.

Huang, J. et al., 2018. Geological Characteristics of Von Kármán Crater, Northwestern South Pole-Aitken Basin: Chang'E-4 Landing Site Region. *Journal of Geophysical Research: Planets*, (1), pp.1–17.

Huang, Y.-H. et al., 2018. No Change in the Recent Lunar Impact Flux Required Based on Modeling of Impact Glass Spherule Age Distributions. *Geophysical Research Letters*.

Huang, Y. et al., 2017. Heterogeneous impact transport on the Moon. *Journal of Geophysical Research: Planets*, (122), pp.1–23.

Ivanov, M.A. et al., 2018. Geology of the Northern Portion of the SPA Basin on the Moon: Evidence for Compositional Stratification of the Ancient Lunar Crust. In *Lunar and Planetary Science Conference*.

Jourdan, F., Mark, D.F. & Verati, C., 2014. Advances in 40 Ar/ 39 Ar dating: from archaeology to planetary sciences – introduction. *Geological Society, London, Special Publications*, 378(1), pp.1–8.

Krüger, T., Kenkmann, T. & Hergarten, S., 2017. Structural uplift and ejecta thickness of lunar mare craters: New insights into the formation of complex crater rims. *Meteoritics and Planetary Science*, 52(10), pp.2220–2240.

Li, L. & Mustard, J.F., 2000. Compositional gradients across mare-highland contacts: Importance and geological implication of lateral transport. *Journal of Geophysical Research*, 105(E8), p.20431.

Li, L. & Mustard, J.F., 2005. On lateral mixing efficiency of lunar regolith. *Journal of Geophysical Research: Planets*, 110(11), pp.1–16.

LSPET, 1972. The Apollo 15 Lunar Samples: A Preliminary Description. Science, 175(4020), pp.363–375.

Maher, B.A., 1988. Magnetic properties of some synthetic sub-micron magnetites. *Geophysical Journal*, 94(1), pp.83–96.

McDougall, I. & Harrison, T.M., 1999. *Geochronology and Thermochronology by the 40Ar/39Ar Method*, Oxford University Press on Demand.

McKay, D. et al., 1991. The lunar regolith. In G. H. Heiken, D. T. Vaniman, & B. M. French, eds. *Lunar Source-Book: A user's guide to the Moon*. New York: Cambridge University Press, pp. 285–356.

McKinnon, W.B. et al., 1997. Cratering on Venus: Models and Observations. In *Venus II: Geology, Geophysics, Atmosphere, and Solar Wind Environment*. p. 969.

Melosh, H.J., 1989. *Impact cratering: A geologic process*, New York: Oxford University.

Melosh, H.J. et al., 2017. South Pole–Aitken basin ejecta reveal the Moon's upper mantle. *Geology*, 45(12), p.1063.

Michael, G., Basilevsky, A. & Neukum, G., 2018. On the history of the early meteoritic bombardment of the Moon: Was there a terminal lunar cataclysm? *Icarus*, 302, pp.80–103.

Michael, G.G., Kneissl, T. & Neesemann, A., 2016. Planetary surface dating from crater size-frequency distribution measurements: Poisson timing analysis. *Icarus*, 277, pp.279–285.

Morbidelli, A. et al., 2012. A sawtooth-like timeline for the first billion years of lunar bombardment. *Earth and Planetary Science Letters*, 355–356, pp.144–151.

Morbidelli, A. et al., 2018. The timeline of the lunar bombardment: Revisited. *Icarus*, 305, pp.262–276.

National Research Council, 2007. Successful response starts with a map: improving geospatial support for disaster management. Washington: National Academies Press.

Neukum, G., 1983. Meteoritenbombardement und Datierung Planetarer Oberflaechen. *Habilitation Dissertation for Faculty Membership, Univ. of Munich*, pp.1–186.

Neukum, G. & Ivanov, B.A., 1994. Crater Size Distributions and Impact Probabilities on Earth from Lunar, Terrestrial-planet, and Asteroid Cratering Data. *Hazards Due to Comets and Asteroids*, 359(1), pp.359–416.

Neukum, G., Ivanov, B.A. & Hartmann, W.K., 2001. Cratering records in the inner solar system in relation to the lunar reference system. *Space Science Reviews*, 96(1–4), pp.55–86.

O'Keefe, J.D. & Ahrens, T.J., 1977. Impact-induced energy partitioning, melting, and vaporization on terrestrial planets. *In: Lunar Science Conference*, 8, p.3357.

Osinski, G.R. & Pierazzo, E., 2012. *Impact cratering: Processes and products*, John Wiley & Sons.

Petro, N.E. & Pieters, C.M., 2004. Surviving the heavy bombardment: Ancient material at the surface of South Pole-Aitken basin. *Journal of Geophysical Research: Planets*, 109(6).

Pierazzo, E. & Melosh, H.J., 2000. Melt production in oblique impacts. *Icarus*, 145, pp.252–261.

Pierazzo, E., Vickery, A.M. & Melosh, H.J., 1997. A reevaluation of impact melt production. *Icarus*, 127(2), pp.408–423.

Pike, R.J., 1977. Apparent depth/apparent diameter relation for lunar craters. *Lunar and Planetary Institute Science Conference Abstracts*, 3, pp.3427–3436.

Potter, R.W.K. et al., 2012. Estimating transient crater size using the crustal annular bulge: Insights from numerical modeling of lunar basin-scale impacts. *Geophysical Research Letters*, 39(18), pp.1–5.

Potts, L. V & von Frese, R.R.B., 2003. Comprehensive mass modeling of the Moon from spectrally correlated free-air and terrain gravity data. *Journal of Geophysical Research*, 108(E4), p.5024.

Ryder, G., 2001. Mass flux during the ancient lunar bombardment: The cataclysm. *32nd Annual Lunar and Planetary Science Conference*.

Ryder, G., Spudis, P.D. & Taylor, G.J., 1989. The case for planetary sample return missions: Origin and evolution of the Moon and its environment. *Eos, Transactions American Geophysical Union*, 70(47), pp.1495–1509.

Shkuratov, Y., 2001. Regolith layer thickness mapping of the Moon by radar and optical data. *Icarus*, 149(2), pp.329–338.

Shuvalov, V. & Dypvik, H., 2013. Distribution of ejecta from small impact craters. *Meteoritics and Planetary Science*, 48(6), pp.1034–1042.

Spudis, P.D., 1993. *The geology of multi-ring impact basins: the Moon and other planets*, Cambridge University Press.

Spudis, P.D. & Sliz, M.U., 2017. Impact melt of the lunar Crisium multiring basin. *Geophysical Research Letters*, 44(3), pp.1260–1265.

Spudis, P.D. & Ryder, G., 1985. Geology and petrology of the Apollo 15 landing site: Past, present, and future understanding. Eos, Transactions American Geophysical Union, 66(43), p.721.

Stöffler, D. et al., 1975. Experimental hypervelocity impact into quartz sand: Distribution and shock metamorphism of ejecta. *Journal of Geophysical Research*, 80(29), pp.4062–

4077.

Stöffler, D., Hamann, C. & Metzler, K., 2017. Shock metamorphism of planetary silicate rocks and sediments: Proposal for an updated classification system. *Meteoritics & Planetary Science*, pp.1–45.

Tera, F., Papanastassiou, D.A. & Wasserburg, G.J., 1974. Isotopic evidence for a terminal lunar cataclysm. *Earth and Planetary Science Letters*, 22(1), pp.1–21.

Tonks, W.B. & Melosh, H.J., 1993. Magma ocean formation due to giant impacts. *Journal of Geophysical Research: Planets*, 98(E3), pp.5319–5333.

Turner, G., Cadogan, P.H. & Yonge, C.J., 1973. Apollo 17 age determinations. *Nature*, 242(5399), pp.513–515.

van der Bogert, C.H. et al., 2018. Constraining the age of the Crisium impact basin. In *European Lunar Symposium*. Toulouse.

Vaniman, D. et al., 1991. Exploration, samples, and recent concepts of the Moon. In G. H. Heiken, D. T. Vaniman, & B. M. French, eds. *Lunar Source-Book: A user's guide to the Moon*. New York: Cambridge University Press, pp. 5–26.

Wartho, J.-A., Kelley, S.P. & Elphick, S.C., 2014. Ar diffusion and solubility measurements in plagioclases using the ultra-violet laser depth-profiling technique. *Geological Society, London, Special Publications*, 378(April 2014), pp.137–154.

Wieczorek, M.A. & Phillips, R.J., 1999. Lunar Multiring Basins and the Cratering Process. *Icarus*, 139, pp.246–259.

Wilhelms, D.E., 1987. *The geologic history of the Moon.*

Wu, W. et al., 2017. The lunar far side soft landing design of "Chang'E-4" mission (Chinese). *Journal of Deep Space Exploration*, 4(2), pp.111–117.

Wünnemann, K., Collins, G.S. & Melosh, H.J., 2006. A strain-based porosity model for use in hydrocode simulations of impacts and implications for transient crater growth in porous targets. *Icarus*, 180(2), pp.514–527.

Wünnemann, K., Collins, G.S. & Osinski, G.R., 2008. Numerical modelling of impact melt production in porous rocks. *Earth and Planetary Science Letters*, 269(3–4), pp.529–538.

Wünnemann, K., Zhu, M.H. & Stöffler, D., 2016. Impacts into quartz sand: Crater formation, shock metamorphism, and ejecta distribution in laboratory experiments and numerical models. *Meteoritics and Planetary Science*, 51(10), pp.1762–1794.

Zhu, M., Wünnemann, K. & Artemieva, N., 2017. Effects of Moon's thermal state on the impact basin ejecta distribution. *Geophysical Research Letters*, 44(22), p.11,211-292,300.

Zhu, M., Wünnemann, K. & Potter, R.W.K., 2015. Journal of Geophysical Research : Planets. *Journal of Geophysical Research E: Planets*, 120, pp.2118–2134.